Recent developments with Cornell's ZEUS-2 spectrometer at APEX

Christopher Rooney, Bo Peng, Gordon Stacey, Thomas Nikola, Amit Vishwas, et al.

Christopher T. Rooney, Bo Peng, Gordon Stacey, Thomas Nikola, Amit Vishwas, Carl Ferkinhoff, Catie Ball, Cody Lamarche, James Higdon, Sarah J. Higdon, "Recent developments with Cornell's ZEUS-2 spectrometer at APEX," Proc. SPIE 12190, Millimeter, Submillimeter, and Far-Infrared Detectors and Instrumentation for Astronomy XI, 121900S (31 August 2022); doi: 10.1117/12.2629453

SPIE.

Event: SPIE Astronomical Telescopes + Instrumentation, 2022, Montréal, Québec, Canada

Recent developments with Cornell's ZEUS-2 spectrometer at APEX

Christopher T Rooney[a], Bo Peng[a], Gordon Stacey[a], Thomas Nikola[a], Amit Vishwas[a], Carl Ferkinhoff[b], Catie Ball[a], Cody Lamarche[c], James Higdon[d], and Sarah J Higdon[d]

[a]Cornell University, Ithaca, NY, USA, 14853
[b]Winona State University, Winona, MN, USA
[c]University of Toledo, Toledo, OH, USA
[d]Georgia Southern University, Statesboro, GA, USA

ABSTRACT

We present recent developments on Cornell's 2nd generation z (redshift) and Early Universe Spectrometer (ZEUS-2). ZEUS-2 is a long-slit echelle-grating spectrometer, originally implemented to deliver R∼1000 spectroscopy in the 350-, and 450-micron telluric windows using NIST Transition-Edge Sensed (TES) bolometer arrays. We have expanded its capabilities to also cover the 200-micron window, and present first-light data for the new array from our 2019 observing campaign on the Atacama Pathfinder EXperiment (APEX) telescope. We also discuss the various enhancements we have implemented to improve observing efficiency and noise performance, including identifying and mitigating vibrations in hardware and improving the stability and robustness of the control software for the detector temperature. Furthermore, we have implemented several software routines to interface with the telescope control systems. These improvements, demonstrated during our recent observing campaign in Nov-Dec 2021, resulted in enhanced reliability and ease of operation, as well as increased sensitivity. A data-driven software pipeline, leveraging data from all 300 detectors on the array to remove common-mode noise, was implemented, and noise performance was further improved by robustly detecting unstable detectors and disabling them during observations.

Keywords: Manuscript format, template, SPIE Proceedings, LaTeX

1. INTRODUCTION

ZEUS-2 was designed as a moderate-resolution, long-slit grating spectrometer with the capability to observe in the 200, 350, and 450 μm telluric windows.[1] The instrument is optimized to study star formation in local and high-redshift galaxies via far-infrared (FIR) fine-structure (FS) lines.[2,3] These lines are important channels of Interstellar Medium (ISM) cooling in star-forming galaxies, and can be used to study galaxy evolution and the physical conditions in the ISM across cosmic time.[4–6] ZEUS-2's moderate resolution of $R \sim 1000$ is well-matched to the typical line widths of these spectral lines ($\sim 200 - 300$ km/s). The ZEUS-2 detector uses Transition Edge Sensors (TESs) with quarter-wavelength backshorts to achieve high sensitivity and quantum efficiency. The instrument utilizes a two-stage GM-cryocooler to cool the optics and readout electronics to 4K, and the detector package, including the TES arrays and multiplexing electronics, is cooled to 120 mK using a two-stage Adiabatic Demagnetization Refrigerator (ADR). For detector readout, we use time-domain multiplexing with the Multi Channel Electronics (MCE) readout system.[7] A photograph of ZEUS-2 with graduate student Christopher Rooney is shown in Fig. 1

ZEUS-2 observes on the Atacama Pathfinder EXperiment (APEX) telescope, where it has been deployed for several observing runs, most recently in 2019 and 2021. In past runs we have detected fine-structure line emission from high-z galaxies, such as G12v2.43,[8] shown in Fig. 1. Following the COVID-19 related shutdown in 2020, our team was able to execute a hybrid observing run with some team members on-site at APEX and others providing remote support. The 2019 observing run was first light for the new 200/600 μm array, which contains an additional 196 detectors at 200 μm and 48 at 600 μm in addition to the 280 detectors at 350/450 μm. With

Further author information: Send correspondence to ctr44@cornell.edu

Millimeter, Submillimeter, and Far-Infrared Detectors and Instrumentation for Astronomy XI, edited by Jonas Zmuidzinas, Jian-Rong Gao, Proc. of SPIE Vol. 12190, 121900S · © 2022 SPIE · 0277-786X · doi: 10.1117/12.2629453

this array functional, ZEUS-2's focal plane is fully populated. In Section 2 we discuss the properties of these arrays with special emphasis on the new arrays. In addition to characterizing our arrays, we have made strides in improving the software that supports our instrument. We have designed a new data reduction pipeline which can robustly handle the many types of noise we see while observing, which we discuss in Section 3.1. During each of our past observing runs, we have identified areas where improvements can be made to our observing efficiency, and, in the past two observing runs especially, we have made several advancements. In particular, Section 3.2 explains our new housekeeping software for temperature monitoring and ADR control, which has improved our observing efficiency significantly, and Section 4 discusses our efforts to maximize ADR hold time via vibration mitigation.

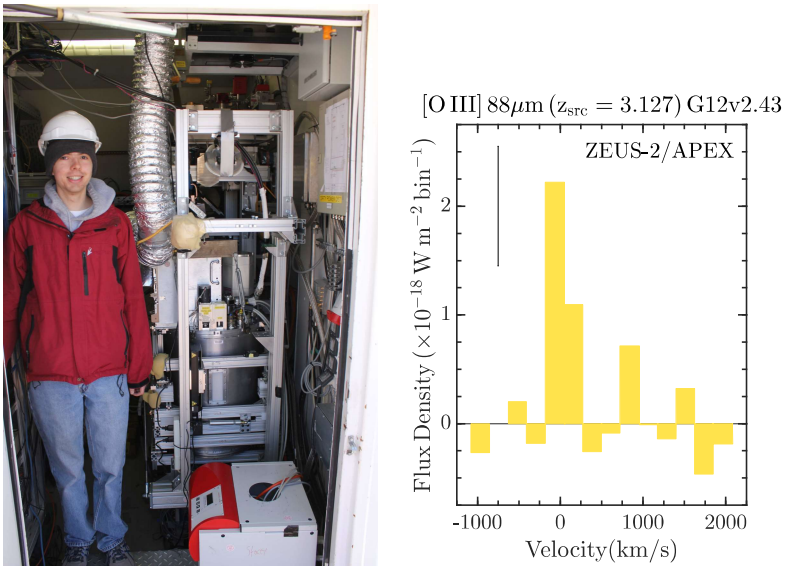

Figure 1. (Left) Photograph of ZEUS-2 on APEX (right) and graduate student Christopher Rooney (left). (Right) [OIII] 88 μm line emission from source G12v2.43 at redshift $z = 3.127$, observed with ZEUS-2 on APEX. Typical 1σ error bar is shown in the upper left. Velocity is with respect to source redshift.[8]

2. ZEUS-2 DETECTOR

2.1 Optical Throughput Calculation

In 2019, ZEUS-2 demonstrated that it is capable of noise performance within $\sim 2\times$ the background limit, $\sim 5 \cdot 10^{-19}$ W m^{-2} (1 sigma, 1 hour) on the sky in good submillimeter weather. To overcome this performance limitation, we are undertaking a thorough review of our instrumental characteristics to identify possible avenues for improvement.

We determine the absolute power being absorbed by a detector by collecting IV curve data under different conditions using standard IV curve scripts[9*]. With IV curve data we can determine the absolute amount of current through each detector and thus the power dissipated via Joule heating. On the superconducting transition, a constant amount of power is transferred to the thermal bath: $P_{bath} = P_{joule} - P_{optical}$. We measure each detector's intrinsic saturation power ($P_{sat} = P_{joule}$ when $P_{optical} = 0$) by mounting a copper plate directly over the detector, isothermal with the detector package to block any optical light falling on them, and taking IV curves at a range of bath temperatures. We also collected IV curves with different optical loads in order to constrain the total instrument throughput. In Fig 2 we show histograms of the saturation powers for the 350/450 μm arrays as well as histograms of optical power received viewing room-temperature and LN2 blackbody sources, and in Fig. 3 we show a histogram of the saturation power on the 200/600 μm arrays and a set of sample power-vs-resistance curves.

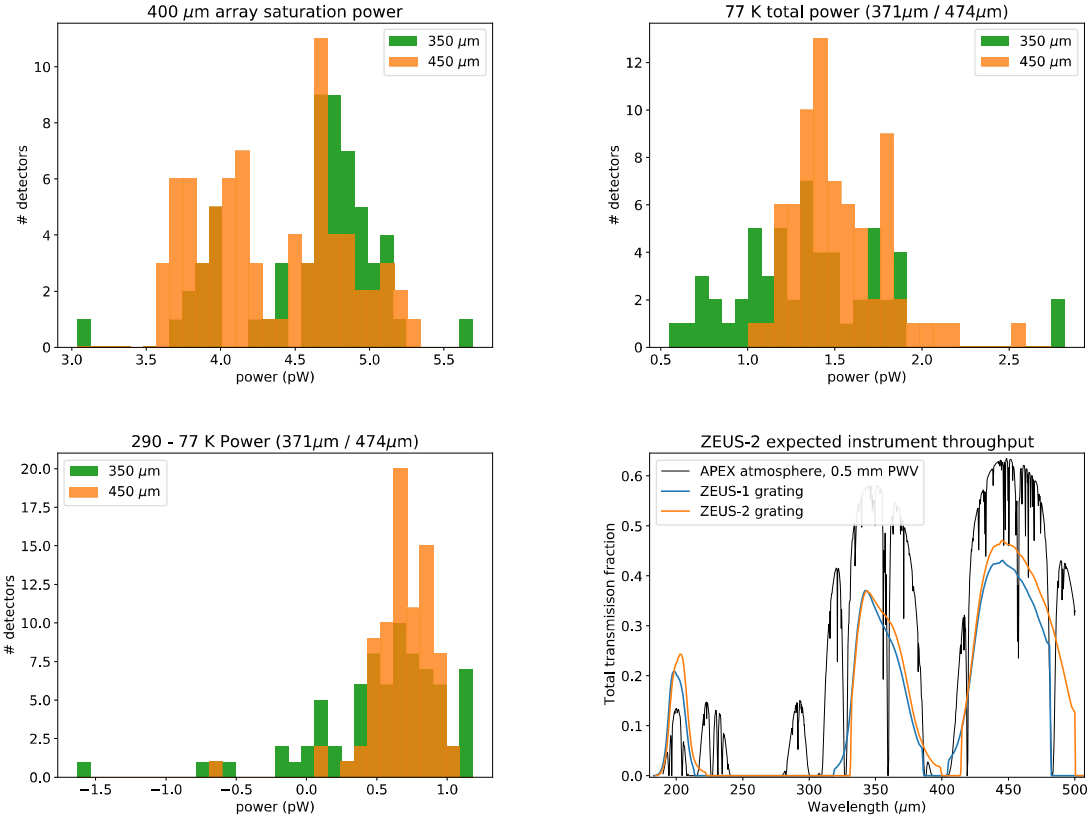

Figure 2. (Top Left) Saturation powers for the detectors on the 350/450 μm arrays at bath temperature $T_{bath} = 130$ mK. Fewer detectors are available on the 350 array due to technical issues encountered while performing dark tests. (Top Right) Power received from a 77 K blackbody, provided by a liquid nitrogen bath. Compared with the dark saturation power we obtain the absolute power received from the source. During this test, the grating illuminated the arrays with 371μm and 474μm radiation on their respective arrays. (Bottom Left) Difference in power between 290 K blackbody (provided by room-temperature Eccosorb) and 77 K blackbody. (Bottom right) Expected cryostat throughput for our three main science observing bands. Because ZEUS-2 is compatible with the grating used in its predecessor ZEUS-1, we plot the expected throughput for both gratings.

In order to calculate the expected power falling on the detectors, we need to first determine the throughput of all the elements in the cryostat optics chain. Many of the filters were designed specifically for ZEUS-2,[10] while others are made of well-studied materials such as Zitex[11] and HDPE.[12] All of the relevant data were collated and combined into a Python module which interpolates the known transmission data for each filter so the total throughput can be computed at arbitrary wavelengths. The results are presented in the lower right of Fig. 2, and sample calculations are provided in Table 1. Using calculated throughput values, the temperatures of our calibration sources, and the optics of the instrument, we calculate the expected power and compare it to the actual power measured. On the 450 μm array at 474 μm we expect $\sim 33\%$ throughput, and measure $\sim 30\%$. On the 350 μm array at 371 μm we expect 21% throughput and measure 9%. At 210 μm we expect 8% due to being near the edge of the bandpass filter, and we measure 2.5%. The worsening efficiencies at smaller wavelengths could indicate a mirror with slightly worse surface accuracy.

There is about a 20% systematic uncertainty in our values due to the uncertainty our system resistances, which include the resistances of the wires in the cryostat and the shunt resistors in parallel with the TESs.

*provided by the UBC MCE group: https://e-mode.phas.ubc.ca/mcewiki/index.php/Main_Page

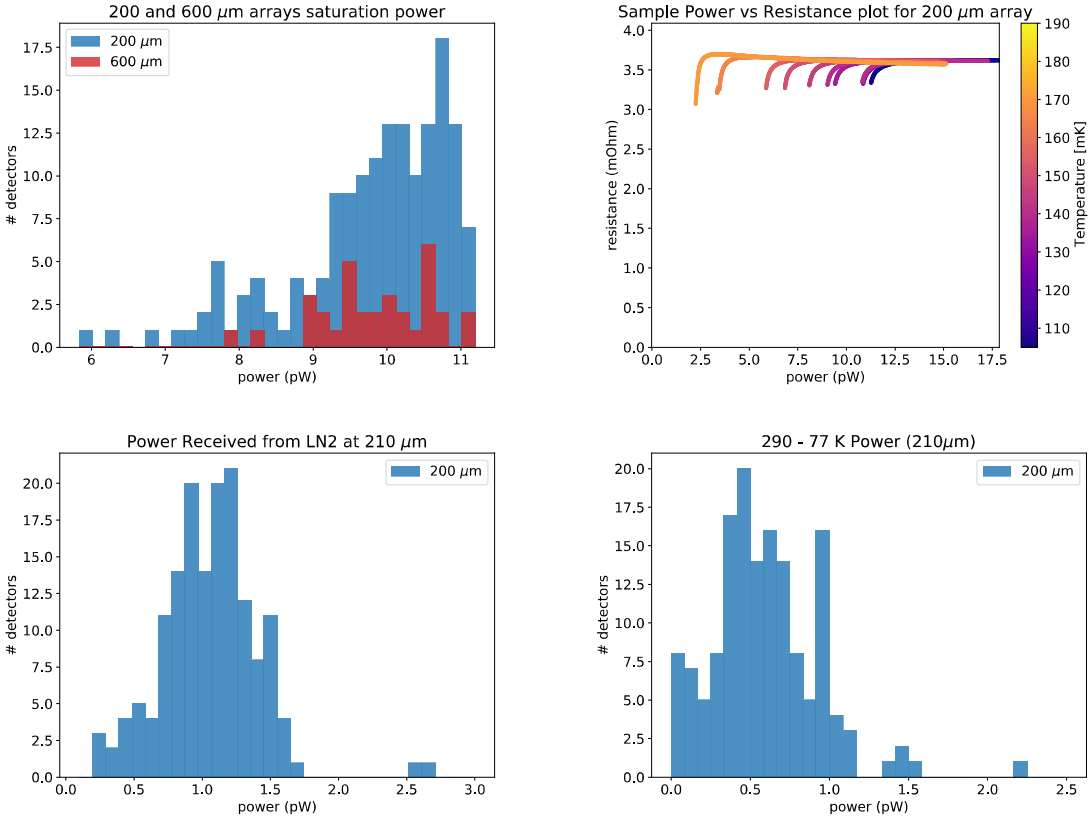

Figure 3. (Top Left) Histogram showing saturation power at $T_{bath} = 130$ mK of the new ZEUS-2 arrays. (Top Right) Sample power-resistance curves for the 200 μm array. The horizontal part of the curve is the normal regime, where the TES acts like a resistor with constant resistance. As dissipated power decreases, the TES enters the transition regime, where dissipated power is constant as resistance decreases. (Bottom Left) Histogram showing total power received from liquid nitrogen at 210 μm. (Bottom Right) Histogram showing power difference between room temperature and liquid nitrogen.

2.2 200 μm array performance

For the first time, we present the characteristics of the new 200 μm and 600 μm arrays. Due to the design of the thermal backshort, these arrays have much more uniform performance. They also have higher saturation powers due to the larger optical loading at 200 μm. Fig 3 shows the values of the saturation power for detectors on these arrays. The mean value of P_{sat} is ~ 10 pW, almost double that of the 350/450 arrays, which show $P_{sat} \sim 5$ pW. By conducting IV curves at a range of bath temperatures, we compute the thermal link conductivity G and the precise critical temperature T_c of the TES by finding the curve of best fit:[13]

$$P_{sat} = G\frac{T_c^n - T_{bath}^n}{n \cdot T_c^{(n-1)}}$$

Figure 4 shows the results of this analysis for all of our detector arrays, and figure 5 shows thermal conductivity G as a function of physical location on the array as well as an example of the curve of best fit used to determine G and T_c. To ensure that our results are physical, we restrict the value of n to $3 < n < 3.5$.

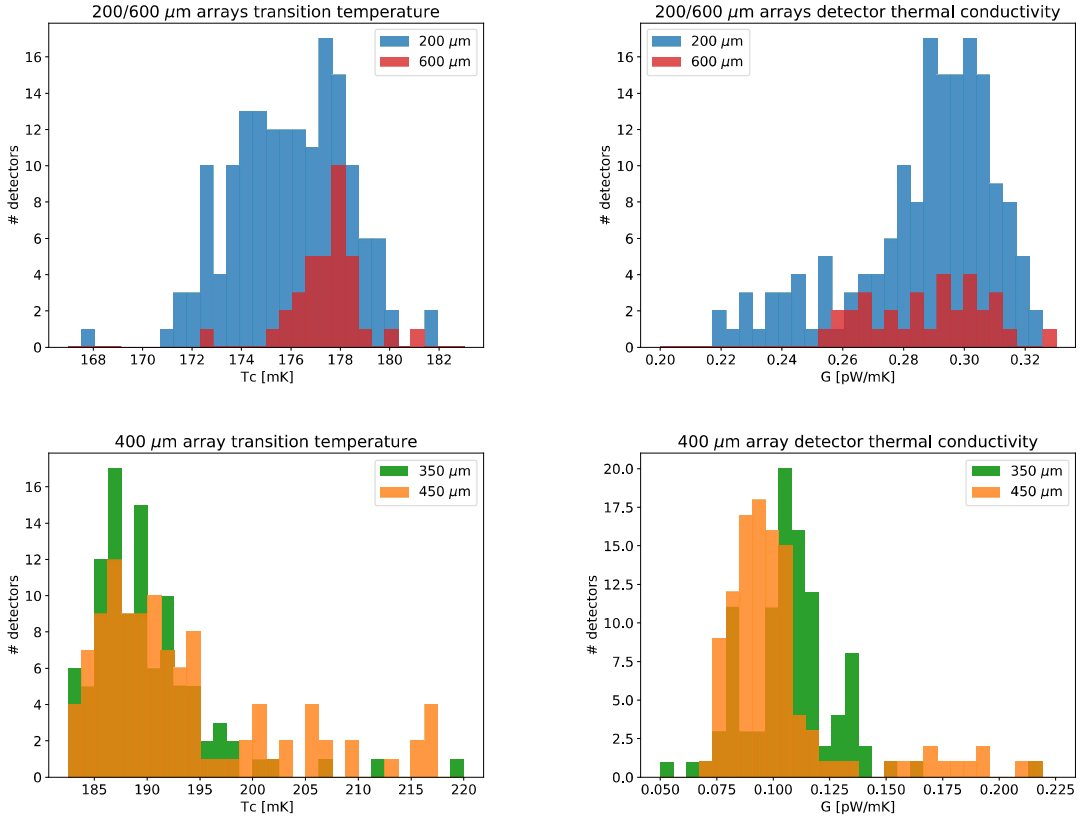

Figure 4. (Left) Histograms showing detector transition temperatures for the new 200 μm and 600 μm arrays (top) and for the 350/450 μm arrays (bottom). (Right) Histograms showing the conductivity of the detector thermal link to the heat bath for the new 200 μm and 600 μm arrays (top) and for the 350/450 μm arrays (bottom).

3. SOFTWARE

3.1 DATA REDUCTION

ZEUS-2 data shows strong correlated noise features that are common between pixels or even across the whole detector array. These noise features have four possible origins: atmospheric noise, external (mechanical) noise, internal (MCE readout) noise, and (MCE column) cross-talk. The atmospheric noise appears as red noise, while all other noise features show up as peaks in the power spectrum. Some of these narrow band noise features can be traced back based on our knowledge of the working frequency of the connected devices, or the scope of their appearance, but the origin of the MCE related noise is not yet fully understood. The frequencies and amplitudes of the MCE related noise change when the MCE parameters such as squid feedback and TES bias are changed, and can also vary over time, making it hard to clean with bandpass filters. These correlated noise features are often at frequencies below 4 Hz, which can introduce excessive noise and ghost power to the chop signal at 2 or 1.75 Hz (ZEUS-2 observes in "wobbler" mode, switching between the science target and empty sky at a rate of ~ 2 Hz, allowing for continuous sky subtraction even in the case of varying atmospheric conditions).

By assuming that the correlated noise in each pixel is a combination of different features at unknown amplitudes, we can use a blind source separation technique to decompose a set of noise-only data into individual noise features. Because these noise features appear in multiple pixels, we use the time series of the off-source pixels as the template to create noise models. Among the popular decomposition algorithms, we choose independent component analysis (ICA)[14] which works by maximizing the non-gaussianity of the noise features. This decomposition method is very effective in separating the correlated noise that show strong frequency dependence, or

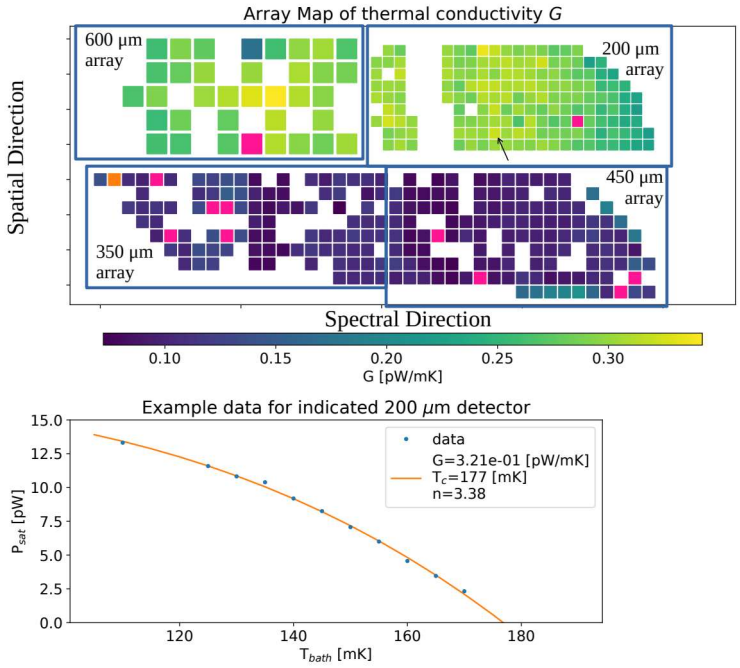

Figure 5. (Top) The layout of the ZEUS-2 array, as projected on sky, colored according to calculated thermal conductivity G in pW/mK. Orange and pink detectors have poorly-fitting curves, while no data is available for white pixels. The array pixel sizes are approximately to scale. Left-to-right in the spectral direction corresponds to increasing wavelength.(Bottom) sample P_{sat} vs T_{bath} data and curve of best fit for spatial position 7/spectral position 10 on the 200 μm array (indicated by black arrow in top fig.)

structure in the time series, while other methods fail to separate frequency-dependent features. The decomposed individual noise features are then fitted together to the time series of on-source pixels and subtracted. Compared with subtracting only the low-frequency features at $f < 0.5$ Hz, the ICA based noise decomposition technique usually shows an improvement on the chop flux error by a factor 1.5 to 3. The process of noise modelling and its effect are illustrated in Fig. 6.

3.2 Thermometry Monitoring and ADR Control

For our 2019 observing run, we implemented a new software to monitor cryostat and detector temperatures, control our ADR magnetization/demagnetization cycle, and operate a feedback loop to keep the detector arrays at a constant temperature. This software was designed to be as robust as possible, as crashes can cause loss of observing time, and even possible damage to equipment if the superconducting ADR magnet is allowed to quench. To accomplish this, a set of Python routines were developed based on the existing control routines that had been implemented in LabView. A LabJack is used for data collection and magnet control, as it has sufficiently precise DACs and ADCs for our purposes. A schematic diagram of our program structure is provided in the left of Fig. 7.

For data storage and remote control, MongoDB is used as an intermediary step. MongoDB is an enterprise-grade database software which is designed for applications that require high uptime, such as website backends, and we find that it is more than sufficient for our needs. MongoDB was chosen due to its flexibility—it allows each document to omit fields easily, which is useful when we are not reading out all of our sensors, and it allows new fields to be added after the fact, simplifying the process of adding new data sources when needed.

Table 1. Sample transmission values for the various elements in our optics chain. Dashes indicate the listed filter is not in the optics chain for the relevant array. The long-pass 50 cm^{-1} appears twice in the 350/450 optics chain: once in the snout (near the Dewar window) and once at the Lyot stop.

wavelength	371 μm	474 μm	205 μm
HDPE Dewar window	0.90	0.94	0.73
Thermal IR filter (c15)	0.97	0.98	0.90
Zitex	0.95	0.95	0.88
Scatter filter	0.95	0.95	0.95
5x cold mirrors[†]	0.94	0.97	0.84
Long-Pass 50 cm^{-1} (k2329)	0.83 (x2)	0.95 (x2)	0.77
Long-Pass 58 cm^{-1} (b688)	—	—	0.91
350 μm BP (k2586)	0.59	—	—
450 μm BP (w1586)	—	0.80	—
200 μm BP (b676)	—	—	0.74
Quantum Efficiency	0.9	0.9	0.92
total	0.22	0.37	0.23

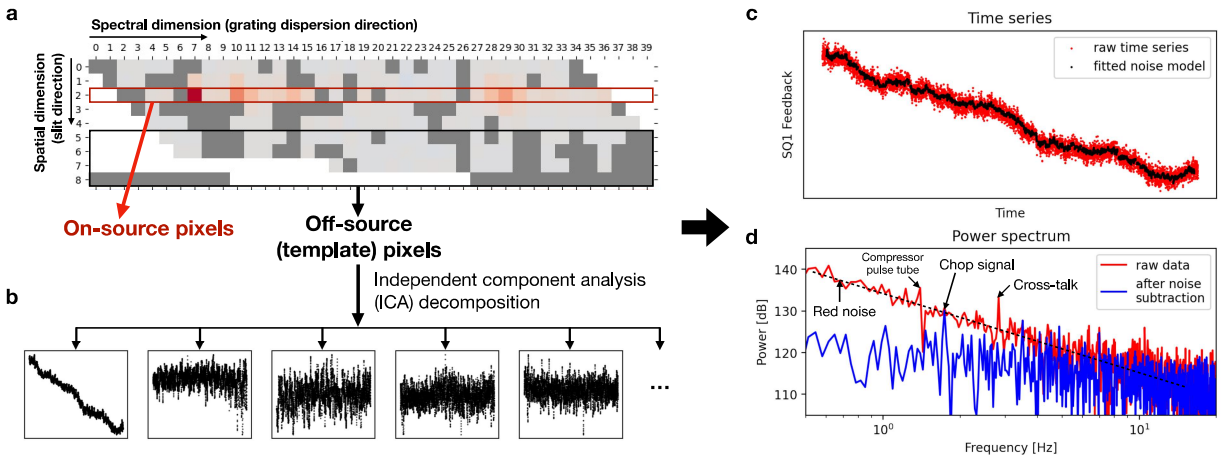

Figure 6. The process of correlated noise subtraction based on ICA. (a) the layout of the detector array is shown with the flux on each pixel of an example spectrum shown in red, and dead pixels masked in dark grey; the red rectangle shows the spatial position where the source is placed, and the black rectangle shows the off-source pixels which are used as noise-only template for ICA decomposition; (b) the example of independent noise features separated by decomposing the time series of the off-source pixels with ICA; (c) the time series of an example on-source pixels; the raw data is plotted in red, and the noise features in (b) are fitted to the raw data and reconstructed as the noise model for this pixel, shown in black; (d) the power spectrum of the raw data (red) and the data after subtracting the noise model (blue); the red noise (black dashed line), external noise from compressor pulse tube (at 1.4 Hz), cross-talk within this MCE column (3 Hz) are strongly suppressed, while the source flux in the chop signal (1.75 Hz) is preserved.

Additionally, the Python module for MongoDB allows for "subscribing" to database updates, so that a routine can be triggered whenever a new document is added. As data is collected, it is processed and uploaded to the database. This triggers update routines in the visualization software, which are used to update a graph of the temperature, so instrument conditions can be monitored in real-time. A sample screenshot of our live plot is provided in the right of Fig. 7. An additional advantage of using this intermediate database is separation of concerns—if the viewing programs experience problems, they will not adversely affect the control program.

Control of the ADR cycle and feedback loop is accomplished by uploading documents to the MongoDB instance when a change in parameters is desired. This allows the main control program to receive the latest

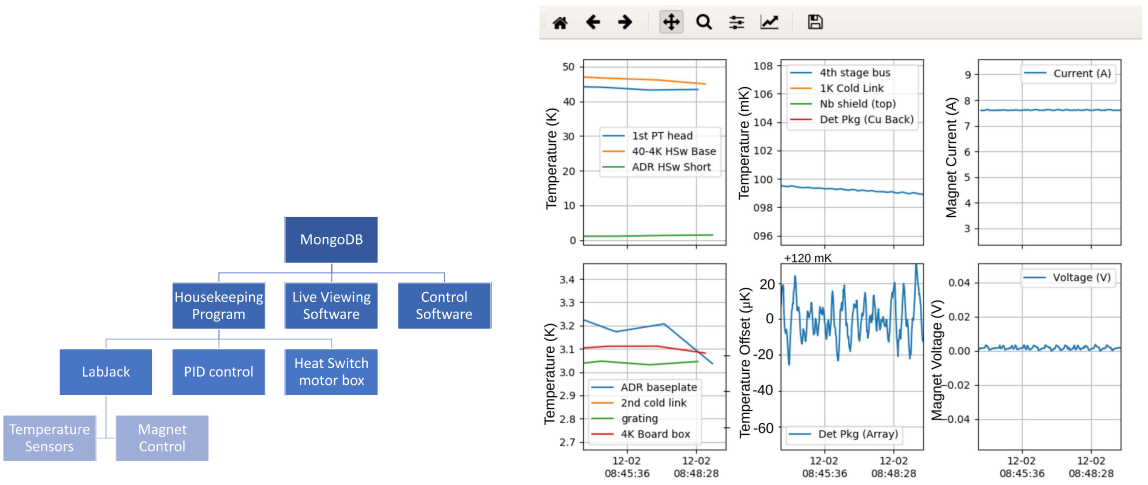

Figure 7. (left) A flowchart diagram demonstrating the structure of our control software. When viewing thermometry data or changing settings, a connection is only made to the MongoDB server, meaning that a crash in the graph software, for example, will not affect the operation of the instrument itself. (right) Example screenshot of the housekeeping graph showing achievable detector package temperature stability, ± 20 μK. While observing, graphs are updated every second to display up-to-date data on the detector and cryostat systems.

parameter changes while maintaining a history of control commands. The current solution interacts with the control software using a JSON file that stores parameters in plain text, significantly reducing network load and allowing us to build more fault tolerance and graceful handling of hardware faults. While the current implementation is command-line based, requiring manual modification of the plain-text parameters file, a light-weight web interface for control of the system is possible.

In order to maintain a constant temperature on the detector package, we utilize a Proportional-Integral-Derivative (PID) feedback loop, which reads the detector temperature and controls the ADR magnet. To increase the detector temperature, a small current can be applied to the ADR magnet. However, the PID loop can become unstable if too much time passes between consecutive data points. Our new software can run the PID loop at ~ 3 Hz, and due to document storage being handled by MongoDB, we have eliminated potential memory leaks that could be caused by retaining too much temperature history in the readout program itself.

Finally, the new software was designed with failure mitigation in mind. If the program does stop unexpectedly, the magnet current is kept constant by the LabJack, which remembers the last command it was given. By inspecting the previously uploaded control commands and thermometry data in the database, the state of the system can be reconstructed and a new settings document uploaded to the database that reflects the current state (thus maintaining continuity and preventing the magnet from quenching). When the control program is started again, it will read the newest settings file before sending commands to the LabJack so that when it does send a command it matches the existing state as closely as possible. All of this allows an interrupted ADR cycle to be continued, minimizing downtime and maximizing observing efficiency.

4. MOUNT HARDWARE REDESIGN

Because of the nature of our detector mount, which consists of several trusses supported by Kevlar threads, our cryostat is more sensitive to vibrations than expected. Because of this, when the cryostat is exposed to even small amounts of vibration (such as a tap on the cryostat shell) the detector will experience heating. This can severely reduce the amount of time our ADR can maintain the necessary cold bath for the detectors. In 2019, we were able to increase our hold time by a factor of > 3 by modifying our mount hardware to eliminate all hard contact points between the APEX mount and our cryostat.

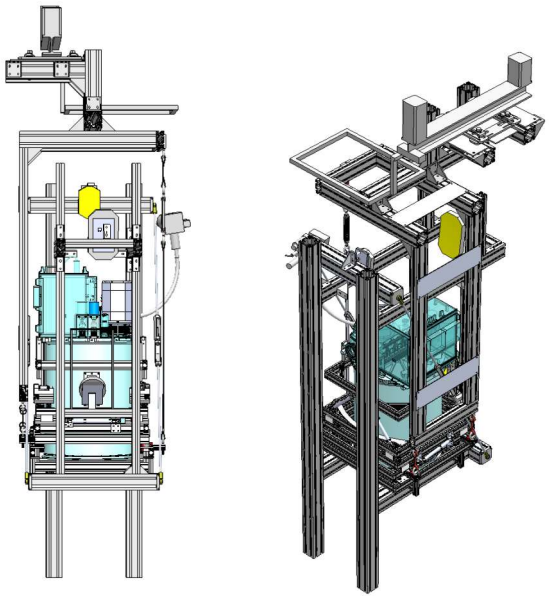

Figure 8. (Left) Side view of new mount design (Right) Isometric view of new mount design.

Motivated by these substantial improvements, we are in the process of redesigning our mount hardware to handle these vibrations. The new mount involves distributing some of the weight of the cryostat onto an I-beam that is present near the top of the APEX A-cabin. This I-beam is quieter in terms of vibrations, but is not guaranteed to be in a constant position with respect to the telescope optics like the dedicated mount points are. Because of this, it was a challenge to design a mount system that takes advantage of the quiet environment of the I-beam while maintaining optical alignment. A drawing of the proposed design is presented in Fig. 8.

5. SUMMARY

ZEUS-2 has demonstrated nearly background-limited performance during observations, but there is still room for improvement. To this end, we have characterized the optical throughput of our system and the physical properties of our detectors, and find that they match their design specifications. The new 200 μm array is online, and preliminary results are encouraging. We improved our software infrastructure, including our thermal monitoring system and data reduction pipeline, to provide better observing efficiency and handle instrumental noise, and finally we are in the process of designing new cryostat mounting hardware that will maximize the cooling power available to the detectors. We are looking forward to a successful observing run at APEX in September.

ACKNOWLEDGMENTS

We acknowledge support from NASA/SOFIA Grant SOF 07-0209. ZEUS-2 was made possible by NSF Grants AST 1716229 and AST 1847892. We are very grateful for support from the APEX team.

REFERENCES

[1] Parshley, S. C., Ferkinhoff, C., Nikola, T., Stacey, G. J., Ade, P. A., and Tucker, C. E., "The optical, mechanical, and thermal design and performance of the 2^{nd} generation redshift (z) and early universe spectrometer, ZEUS-2," in [*Millimeter, Submillimeter, and Far-Infrared Detectors and Instrumentation for Astronomy VI*], Holland, W. S. and Zmuidzinas, J., eds., *Society of Photo-Optical Instrumentation Engineers (SPIE) Conference Series* **8452**, 84521R (Sept. 2012).

[2] Ferkinhoff, C., Nikola, T., Parshley, S. C., Stacey, G. J., Irwin, K. D., Cho, H.-M., and Halpern, M., "Zeus-2: a second generation submillimeter grating spectrometer for exploring distant galaxies," in [*Proceedings of the SPIE, Volume 7741, id. 77410Y (2010).*], **7741** (July 2010).

[3] Ferkinhoff, C., Nikola, T., Parshley, S. C., Stacey, G. J., Irwin, K. D., Cho, H.-M., Niemack, M., Halpern, M., Hasselfield, M., and Amiri, M., "Design and first-light performance of tes bolometer arrays for submillimeter spectroscopy with zeus-2," in [*Millimeter, Submillimeter, and Far-Infrared Detectors and Instrumentation for Astronomy VI. Proceedings of the SPIE, Volume 8452, article id. 845207, 12 pp. (2012).*], **8452** (September 2012).

[4] Stacey, G. J., "THz Low Resolution Spectroscopy for Astronomy," *IEEE Transactions on Terahertz Science and Technology* **1**, 241–255 (Sept. 2011).

[5] Lamarche, C., Verma, A., Vishwas, A., Stacey, G. J., Brisbin, D., Ferkinhoff, C., Nikola, T., Higdon, S. J. U., Higdon, J., and Tecza, M., "Resolving Star Formation on Subkiloparsec Scales in the High-redshift Galaxy SDP.11 Using Gravitational Lensing," *ApJ* **867**, 140 (Nov. 2018).

[6] Peng, B., Lamarche, C., Stacey, G. J., Nikola, T., Vishwas, A., Ferkinhoff, C., Rooney, C., Ball, C., Brisbin, D., Higdon, J., and Higdon, S. J. U., "Far-Infrared Line Diagnostics: Improving N/O Abundance Estimates for Dusty Galaxies," *ApJ* **908**, 166 (Feb. 2021).

[7] Battistelli, E. S., Amiri, M., Burger, B., Halpern, M., Knotek, S., Ellis, M., Gao, X., Kelly, D., Macintosh, M., Irwin, K., and Reintsema, C., "Functional Description of Read-out Electronics for Time-Domain Multiplexed Bolometers for Millimeter and Sub-millimeter Astronomy," *Journal of Low Temperature Physics* **151**, 908–914 (May 2008).

[8] Vishwas, A., Ferkinhoff, C., Nikola, T., Parshley, S. C., Schoenwald, J. P., Stacey, G. J., Higdon, S. J. U., Higdon, J. L., Weiss, A., Güsten, R., and Menten, K. M., "Detection of [O III] at z $\sim$ 3: A Galaxy Above the Main Sequence, Rapidly Assembling Its Stellar Mass," *ApJ* **856**, 174 (Apr. 2018).

[9] Battistelli, E. S., Amiri, M., Burger, B., Devlin, M. J., Dicker, S. R., Doriese, W. B., Dünner, R., Fisher, R. P., Fowler, J. W., Halpern, M., Hasselfield, M., Hilton, G. C., Hincks, A. D., Irwin, K. D., Kaul, M., Klein, J., Knotek, S., Lau, J. M., Limon, M., Marriage, T. A., Niemack, M. D., Page, L., Reintsema, C. D., Staggs, S. T., Swetz, D. S., Switzer, E. R., Thornton, R. J., and Zhao, Y., "Automated SQUID tuning procedure for kilo-pixel arrays of TES bolometers on the Atacama Cosmology Telescope," in [*Millimeter and Submillimeter Detectors and Instrumentation for Astronomy IV*], Duncan, W. D., Holland, W. S., Withington, S., and Zmuidzinas, J., eds., *Society of Photo-Optical Instrumentation Engineers (SPIE) Conference Series* **7020**, 702028 (July 2008).

[10] Vishwas, A., *Ground based THz Spectroscopy of Obscured Starbursts in the Early Universe enabled by the 2nd generation z(Redshift) & Early Universe Spectrometer*, PhD thesis, Cornell University, New York (May 2019).

[11] Benford, D. J., Gaidis, M. C., and Kooi, J. W., "Transmission Properties of Zitex in the Infrared to Submillimeter," in [*Tenth International Symposium on Space Terahertz Technology*], Crowe, T. W. and Weikle, R. M., eds., 405 (Mar. 1999).

[12] Birch, J. R., Dromey, J. D., and Lesurf, J., "The optical constants of some common low-loss polymers between 4 and 40 cm $^{-1}$," *Infrared Physics* **21**, 225–228 (July 1981).

[13] Irwin, K. D. and Hilton, G. C., [*Transition-Edge Sensors*], 63 (2005).

[14] Hyvärinen, A. and Oja, E., "Independent component analysis: algorithms and applications. Neural networks," **13**(4-5), 411–430 (2000).